*Human Molecular Genetics*, 2016, Vol. 25, No. 13 2672–2680

**doi: 10.1093/hmg/ddw126**
Advance Access Publication Date: 18 May 2016
Original Article

ORIGINAL ARTICLE

# *BESTROPHIN1* mutations cause defective chloride conductance in patient stem cell-derived RPE

Yasmin Moshfegh[1,2], Gabriel Velez[3,4,5], Yao Li[2], Alexander G. Bassuk[6], Vinit B. Mahajan[4,5] and Stephen H. Tsang[1,2,*]

[1]Barbara & Donald Jonas Laboratory of Regenerative Medicine, and Bernard & Shirlee Brown Glaucoma Laboratory, Department of Pathology & Cell Biology, Institute of Human Nutrition, College of Physicians and Surgeons, Columbia University, New York, NY 10032, USA [2]Edward S. Harkness Eye Institute, New York-Presbyterian Hospital, New York, NY 10032, USA [3]Omics Lab, [4]Department of Ophthalmology and Visual Sciences, [5]Medical Scientist Training Program and [6]Department of Pediatrics, University of Iowa, Iowa City, IA, USA

*To whom correspondence should be addressed at: Edward S. Harkness Eye Institute, New York-Presbyterian Hospital/Columbia University Medical Center, 635 West 165th Street, Box 112, New York, NY 10032, USA. Tel: +212-342-1186; Fax: +212-305-4987; Email: sht2@columbia.edu

## Abstract

Bestrophin1 (BEST1) is expressed in human retinal pigment epithelium (RPE) and mutations in the *BEST1* gene commonly cause retinal dysfunction and macular degeneration. BEST1 is presumed to assemble into a calcium-activated chloride channel and be involved in chloride transport but there is no direct evidence in live human RPE cells to support this idea. To test whether BEST1 functions as a chloride channel in living tissue, BEST1-mutant RPE (R218H, L234P, A243T) were generated from patient-derived induced pluripotent stem cells and compared with wild-type RPE in a retinal environment, using a biosensor that visualizes calcium-induced chloride ion flux in the cell. Calcium stimulation elicited chloride ion export in normal RPE but not in RPE derived from three patients with *BEST1* mutations. These data, along with three-dimensional modeling, provide evidence that BEST1 assembles into a key calcium-sensing chloride channel in human RPE.

## Introduction

Channelopathies are diseases due to mutations in channels that transport ions across cell membranes (1). To develop targeted therapies to specific channelopathies, it is crucial to understand precisely how disease mutations affect ion conductance. Vitelliform macular degeneration (VMD, OMIM#153700) is a blinding, retinal channelopathy caused by mutations in *BESTROPHIN1* (*BEST1*, MIM#607854) (2,3). The gene product BESTROPHIN1 (BEST1) is thought to comprise a transmembrane anion channel expressed at the basolateral membrane of human retinal pigment epithelium (RPE) (4). It is also speculated that BEST1 is the $Ca^{2+}$-activated chloride channel (CaCC) responsible for the electrooculogram (EOG) light peak (5,6). Still the question remains whether BEST1 functions as a chloride ($Cl^-$) channel directly or indirectly regulates $Cl^-$ conductance via another channel (7–10).

In human VMD caused by *BEST* mutations, $H_2O$ and lipofuscin accumulate under the retina (11) and the EOG light peak is deficient (12). But *Best1* knockout mice show normal RPE CaCC activity and EOG responses (13–16), so controversy remains regarding the true function of BEST1 in human RPE. Also, some studies claim that BEST1 regulates $Cl^-$ uptake into the endoplasmic reticulum (ER) (6,15,17,18), while others suggest BEST1 regulates $Cl^-$ efflux at the basal lateral plasma membrane (19). This issue is also unresolved, since previous studies were

**Received:** February 2, 2016. **Revised:** April 13, 2016. **Accepted:** April 18, 2016

© The Author 2016. Published by Oxford University Press.
All rights reserved. For permissions, please e-mail: journals.permissions@oup.com

limited by the use of heterologous cell lines and indirect methods of $Cl^-$ ion detection (20,21). Many previous studies of chloride current through bestrophin channels employed whole-cell, patch-clamp analysis of exogenously overexpressing HEK293 cells (21,22).

To circumvent the limits of heterologous cells and inconsistency of model organisms (23–27), we used patient-specific RPE (iRPE) and a novel physiological approach to visualize $Cl^-$ ions in RPE directly with a biosensor. With this method, BEST1 can be directly studied in real-time, in a native RPE environment with endogenous BEST1 expression, providing strong evidence that BEST1 is a key calcium-sensing chloride channel in human RPE, and essential for RPE viability.

## Results

### RPE derived from *BEST1* mutant patients

Patients with *BEST1* mutations display characteristic retinal morphology and electrographic abnormalities suggesting defects in RPE fluid transport. We took advantage of this set of symptoms to uncover *BEST1* mutations. An R218H mutation was detected in a 52-year-old with probable lipofuscin deposition (vitelliform lesion), a thin photoreceptor layer and diseased RPE with extensive subretinal serous fluid (Fig. 1B). A second A243T mutation was in a 61-year-old male who had retinal atrophy and disintegration of the photoreceptor mitochondrial band (Fig. 1C), indicating phagocytosis by the RPE had disrupted the outer segment. Mutations in R218 and A243 are known to cause BEST1-VMD (19). The third mutation was a previously undescribed substitution, L234P, in a 7-year-old boy with vitelliform lesions in both eyes, subretinal serous fluid and retinal outer segment debris (Fig. 1D). Each subject showed evidence of defective RPE fluid transport, a mutation in *BEST1* and electrophysiological changes consistent with BEST1 VMD (Fig. 1E). We derived induced pluripotent stem cells from these patients to generate functional RPE carrying mutant BEST1 (Fig. 1F and G); these cells allow direct measurement of the effect of VMD *BEST1* mutations on chloride ion transport across the RPE cell membrane.

### Structural modeling of human BEST1 mutations

BEST1 is well conserved among species, especially in the N-terminal region, where many *BEST1* missense mutations occur (28,29). Our patients' mutations were in two adjacent alpha-helices, S3a and S3b, at residues conserved across seven species (Fig. 2A). To assess conservation of these residues, a PSI-BLAST identified 493 homologous sequences and ConSurf analysis was performed on the 150 sequences with the lowest E values. This analysis showed a minimum of 35% conservation between 150 bestrophin sequences. The residues mutated in our three patients had percent identity values of 97% (R218), 99% (A243) and 100% (L234) across 150 bestrophin sequences. The high degree of conservation highlights the probable importance of these amino acids for BEST1 function.

High-resolution crystal structures exist for *Klebsiella pneumoniae* BEST1 (22) and chicken BEST1 (30) but the crystal structure of human BEST1 (hBEST1) remains undetermined. To predict how our patients' mutations compromise the function of the hBEST1 channel, we generated three-dimensional models from previously solved crystal structures (Fig. 2B and C). Our hBEST1 model oriented the mutated residues along the channel pore interior, at the interface between adjacent hBEST1 subunits (Fig. 2D). Thus, the patient mutations were predicted to disrupt the stability of pentamer formation and affect channel function.

We modeled how individual mutations might affect hBEST1 function. R218H falls on a putative $Cl^-$ binding site in the bestrophin channel inner cavity (30). This binding site forms at the interface of three residues (R105, R218 and T219) on two adjacent helical subunits (Helix S2b and S2c; Fig. 2E). The arginine to histidine substitution appeared to shift the distance between the $Cl^-$-binding residue and the anion and may decrease the local concentration of ions at the neck of the channel pore, thereby disrupting anion selectivity. Analysis of the hBEST1 electrostatic potential showed the residues surrounding the mutation change from a positive to a neutral charge, suggesting they bind less tightly to negatively charged ions, i.e. $Cl^-$ (Fig. 2F). Also, R218 appeared to be involved in a hydrogen-bonding network on the interface of two subunits, further highlighting that this mutation destabilizes the pentamer. The L234P mutation was in a buried $\alpha$-helix that would likely be disrupted by a proline substitution, causing structural defects at the channel interface (Fig. 2G–H). The A243T mutation falls on helix S4a, which sits in a hydrophobic pocket that is partially embedded in the membrane. A substitution from a hydrophobic residue to a polar uncharged residue (Fig. 2J) could disrupt the association between adjacent subunits and potentially between the channel and the membrane. This three-dimensional modeling suggested the disease mutations reduce $Cl^-$ conductance, either by directly altering conductance or affecting the stability and formation of the hBEST1 pentamer.

### $Cl^-$ current imaging of patient-derived RPE

To test if BEST1 directly controls $Cl^-$ conductance in patient RPE cells, we performed live-cell imaging with a fluorescent anion biosensor (31). This biosensor is sensitive to $Cl^-$, so that when intracellular [$Cl^-$] increases, its YFP intensity drops, and vice versa (31). $Cl^-$ currents were measured in control and *BEST1* mutant patient-derived RPE cells. Since BEST1 is predicted to be calcium-activated, the $Ca^{2+}$ ionophore A23187 (32) was used to induce $Ca^{2+}$ release from the ER and activate BEST1. Within 3 min of stimulation, wild-type (WT) RPE cells expressing the biosensor exhibited a decreased concentration of intracellular $Cl^-$, followed by recovery within 15 min (Fig. 3A, Supplementary Material, Movie S1). In contrast, RPE cells derived from patients with *BEST1* mutations (Fig. 1F) did not respond to this stimulation (Fig. 3B–D, Supplementary Material, Movies S2–S4), suggesting BEST1 mediates an efflux of $Cl^-$ in human RPE.

BEST1 has been hypothesized to function as an intracellular channel that conducts $Cl^-$ as the counter-ion that facilitates $Ca^{2+}$ reentry into the ER (33,34). Based on the biosensor readout in WT RPE, intracellular $Ca^{2+}$ release caused intracellular [$Cl^-$] to drop. To test whether $Cl^-$ ions were moving out of the basolateral membrane or into the ER, the $Cl^-$ biosensor was targeted to the ER with an ER-localization signal sequence and KDEL (Lys-Asp-Glu-Leu) motif. Under the same stimulation and imaging conditions in WT RPE cells, we detected no significant change in [$Cl^-$] in the ER (Fig. 4A). This negative result supports a model in which BEST1 does not function at the ER but instead conducts $Cl^-$ across the cell membrane (Fig. 4B).

## Discussion

To develop effective therapies for the BEST1 VMD channelopathy, it is crucial to determine the mechanism linking genetic mutations to eye disease. Our novel biosensor imaging and

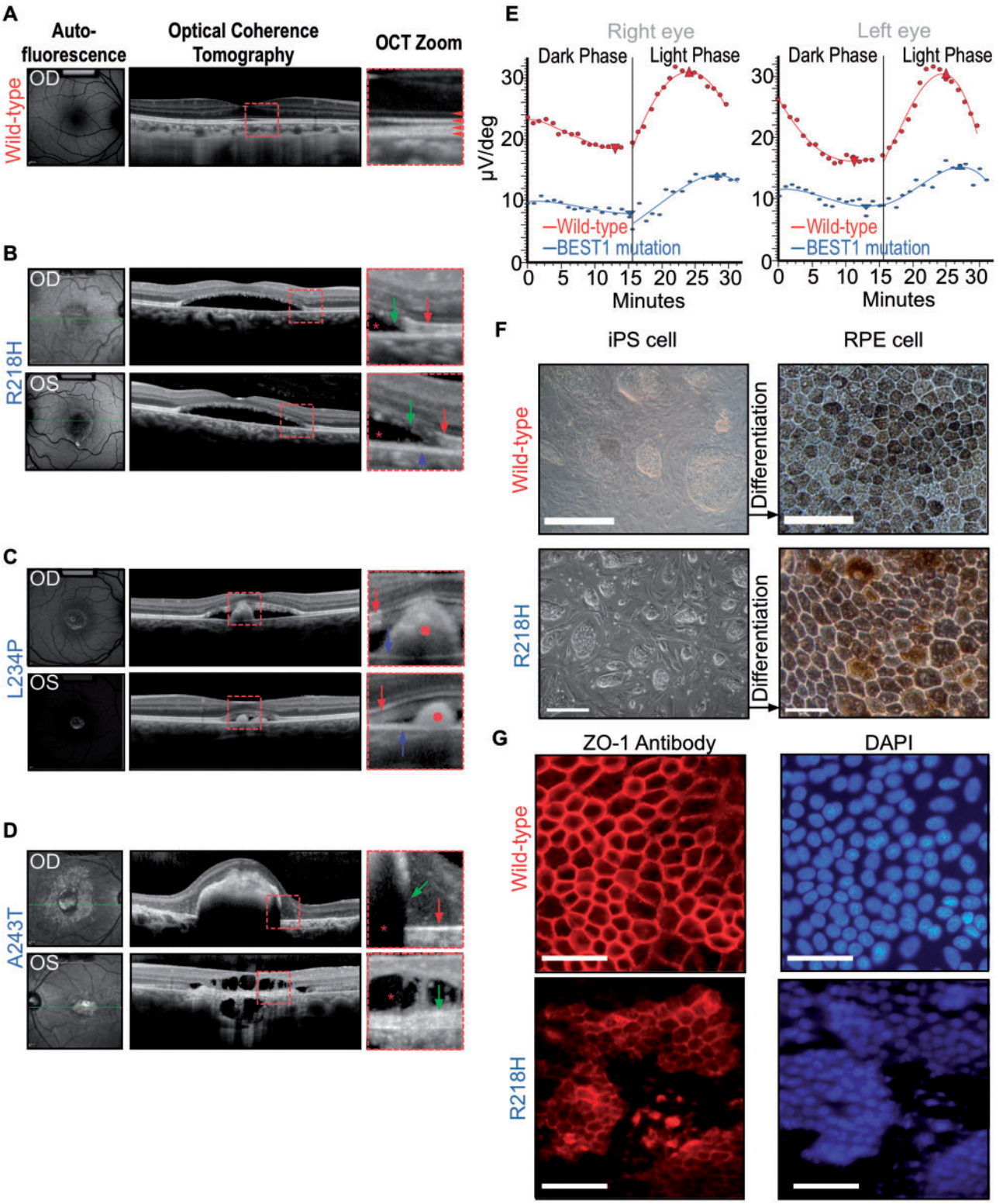


**Figure 1.** Human *BEST1* mutations cause defective fluid transport in RPE and accumulation of serous fluid (*) in the subretinal space with a defective EOG light peak. **(A)** Autofluorescence and optical coherence tomography (OCT) images from a normal eye. Red square shows zoomed in area (right panel). Red arrowheads point to the four distinct reflective bands of the outer retinal layers in a normal eye under OCT scan. From top to bottom: external limiting membrane—boundary between photoreceptor nuclei and inner segments; EZ (ellipsoid zone)—formed by mitochondria in the outer portion of photoreceptor inner segments; interdigitation zone—where photoreceptor outer segments (POSs) interface with the RPE; RPE (retinal pigmented epithelium). **(B)** Phenotypic manifestation in a 52-yo VMD patient with R218H mutation. Right (OD) and left (OS) eyes showed vitelliform lesions. The central photoreceptor layer is thin compared with that of a healthy control with a loss of integrity of the retinal bands, and serous fluid has developed subretinally in OCT imaging. Green arrows point to POS debris due to diseased RPE. Red arrows point to EZ. Blue arrow points to RPE layer. Red star marks the subretinal fluid accumulation. **(C)** Phenotypic manifestation in a 7-yo VMD patient with L234P mutation. Right and

computer modeling provide strong evidence that BEST1 is a $Ca^{2+}$-activated $Cl^-$ channel, and VMD patient-derived *BEST1*-mutant RPE are defective in conducting $Cl^-$. The phenotype only occurs in human RPE and not in mice likely because of cell and species-specific expression. Recently, it was shown that Best1 is expressed in mouse testes (not in mouse RPE), and that it's exclusively localized in the cell membrane of human RPE (25).

Our structural models place the three VMD mutations at the interface between hBEST1 subunits. The residues at this interface are highly conserved across bestrophin sequences, likely because bonding interactions stabilize the multimeric structures. In contrast to mutations that disrupt channel assembly at the interface, the R218H mutation appears likely to disrupt anion selectivity along the pore, affecting chloride conductance directly. Other channelopathy studies have similarly highlighted how structural modeling can reveal disease mechanisms. For example, class II mutants of Cystic Fibrosis Transmembrane Conductance Regulator (e.g. ΔF508) likely form an unstable channel because they cannot fold correctly, contributing to development of cystic fibrosis (35). Similarly, predicted misfolding of the $Ca_v2.1$ subunit of P/Q-type $Ca^{2+}$ channels likely causes episodic ataxia type-2 (EA2) (36).

Several types of BEST1 disease mutations prevent it from localizing normally to the basal cell membrane (25,37). The A243T mutant appears to be defective in $Cl^-$ conductance (38) because of mislocalization (37). This mutant may be analogous to a Y227N mutant, believed not to translocate efficiently to the basal membrane (39). In contrast, a nearby R218H mutation has no effect on membrane localization yet still causes the mutant phenotype (40–42). Structural modeling placed residue 218 within the channel pore, suggesting this mutation disrupts a $Cl^-$ binding site and renders BEST1 channels defective in conductance. Another novel mutation we described, L234P changes a highly conserved residue (Fig. 2F) near other disease mutations (Y227N, T237R, Q238R) that mislocalize to the cytoplasm (25,37). Chloride flux is likely blocked in *BEST1*-mutant RPE because of BEST1 channel mislocalization, anion transport or binding defects, or a combination of both (43). Detailed studies of BEST1 localization (25,37) also confirm this cell biological basis of dysfunction.

All three patient-specific RPE are defective in $Cl^-$ ion efflux in our biosensor assay and VMD mutations directly affect BEST1 in regulating $Cl^-$ exchange in the cell membrane. Since dark-adapted photoreceptors metabolize each molecule of glucose into six molecules of $H_2O$ and $CO_2$, $H_2O$ accumulation is prevented by $Cl^-$ outflux in the basolateral membrane, which drives osmotic transport of $H_2O$ across RPE via aquaporins (34). In VMD, $Cl^-$ outflux is defective, preventing the $Cl^-$ driven transport of water and weakening adhesion of the RPE to the neuronal retina (44). Thus, therapies for BEST1 channelopathy should restore $Cl^-$ conductance in the RPE, to prevent subretinal $H_2O$ accumulation.

## Materials and Methods

### Live imaging

The collection of data used in this study was approved by the Institutional Review Board for Human Subjects Research at Columbia University Medical Center, was compliant with the Health Insurance Portability and Accountability Act and adhered to the tenets of the Declaration of Helsinki. Written informed consent was received from participants. Clinical examination and genetic testing was performed as previously described (45,46). Stereoscopic autoflourescent images and spectral domain optical coherence tomography were obtained using Spectralis Heidelberg (Heidelberg, Germany)

### Homology modeling of human bestrophin-1

Homology models for hBEST1 were generated using MODELLER 9.14, as described previously (47,48). Briefly, a BLAST search for hBEST1 against the Protein Database (PDB) returned the structure of chicken BEST1 (PDB ID 4RDQ) as the top hit (Supplementary Material, Table S1). Ten models were generated using each template and superimposed well with a root mean square deviation that was $<0.257$ over 307 $C_\alpha$ atoms (Supplementary Material, Figure S1A. and B and Table S2). PyMOL and UCSF Chimera (49) were used to generate all structure figures (http://www.pymol.org/). Modeling of the channel pore surface was performed in MOLE 2.0 (50). Electrostatic potentials were calculated in APBS (51). Sequence alignments were performed using Geneious R8 (52).

#### *Generation of patient iPSC*

CytoTune-iPS Sendai Reprogramming Kit (53) (Life Technologies, Carlsbad, CA), was used to generate iPS with no genomic integration viral remnants. The iPSCs underwent four quality-control tests: karyotyping, genome sequencing (54), testing for the absence of Yamanaka transgenes and a pluripotency assay.

#### *Differentiation of patient iPSCs into RPE*

Human iPSCs were differentiated into RPE as we had done before (53). Phenotype was confirmed by assaying RPE-specific features: i) pigment expression and hexagonal cell shape (morphology), ii) expression of apical-basal polarity markers, iii) expression of RPE-specific markers (qPCR and immunoassays) and iv) phagocytic activity (data not shown). Primary antibodies are anti-RPE65 (rabbit, Santa Cruz; mouse, GeneTex), rabbit anti-bestrophin (Abcam) and rabbit anti-ZO-1 (Zymed).

**Figure 1.** Continued

left eyes showed vitelliform lesions. Subretinal fluid and outer segment debris are visible in the SD-OCT images. Red circles mark POS debris due to diseased RPE. Red arrows point to EZ. Blue arrows point to RPE.**(D)** Phenotypic manifestation in a 61-yo VMD patient with A243T mutation; Photoreceptor bands have disintegrated at various points. Red star indicates subretinal fluid accumulation. Green arrows point to POS debris due to diseased RPE. Red arrow points to EZ (upper panel). **(E)** A reduction in EOG light rise is seen in BEST1 VMD. Light-rise of the EOG is generated by $Cl^-$ mediated depolarization of the basal membrane of the RPE. The graphs show mean EOG responses to light of a normal (red line) and a VMD patient with R218H mutation (blue line). The normal increase in electrical response to light began after ~15 min and reached a peak after 25 min. In the mutant case, this light rise response is both attenuated and slower. **(F)** Characteristic light microscopy images of cultured iPSCs from a WT control (top panels) and from the R218H patient in A before differentiation (left), and the RPE cells derived from these iPS after 12 weeks of differentiation (right). Scale bar: 100 μm. **(G)** Characteristic RPE cultures from a WT control (top panels) and the R218H patient (bottom panels) immunolabeled for the epithelial specific tight junction marker ZO-1 (left) with a corresponding DAPI (nuclear) stain (right). Scale bar: 100 μm.

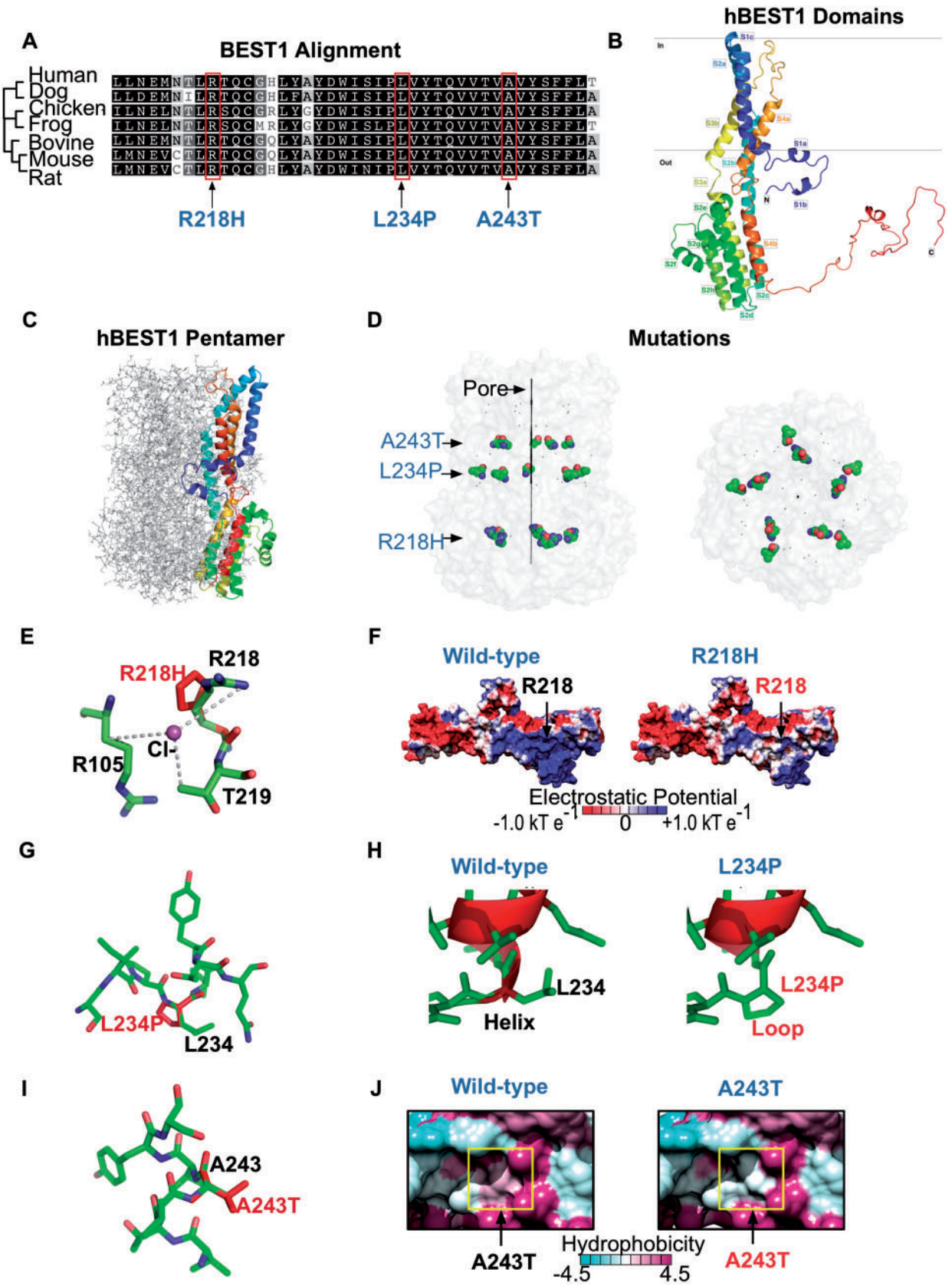


Figure 2. Modeling of VMD mutations on human bestrophin-1 structure. **(A)** Species sequence alignments of BEST1 shows that the patient VMD mutations fell on conserved residues. **(B)** Homology model of hBEST1 generated using cBEST1 (PDB: 4RDQ) as a template. **(C)** Superimposition of the hBEST1 monomer on the channel pentamer. **(D)** Location of the patient VMD mutations in relationship to the channel pore. **(E)** Visualization of the putative $Cl^-$-binding site in hBEST1 formed by the

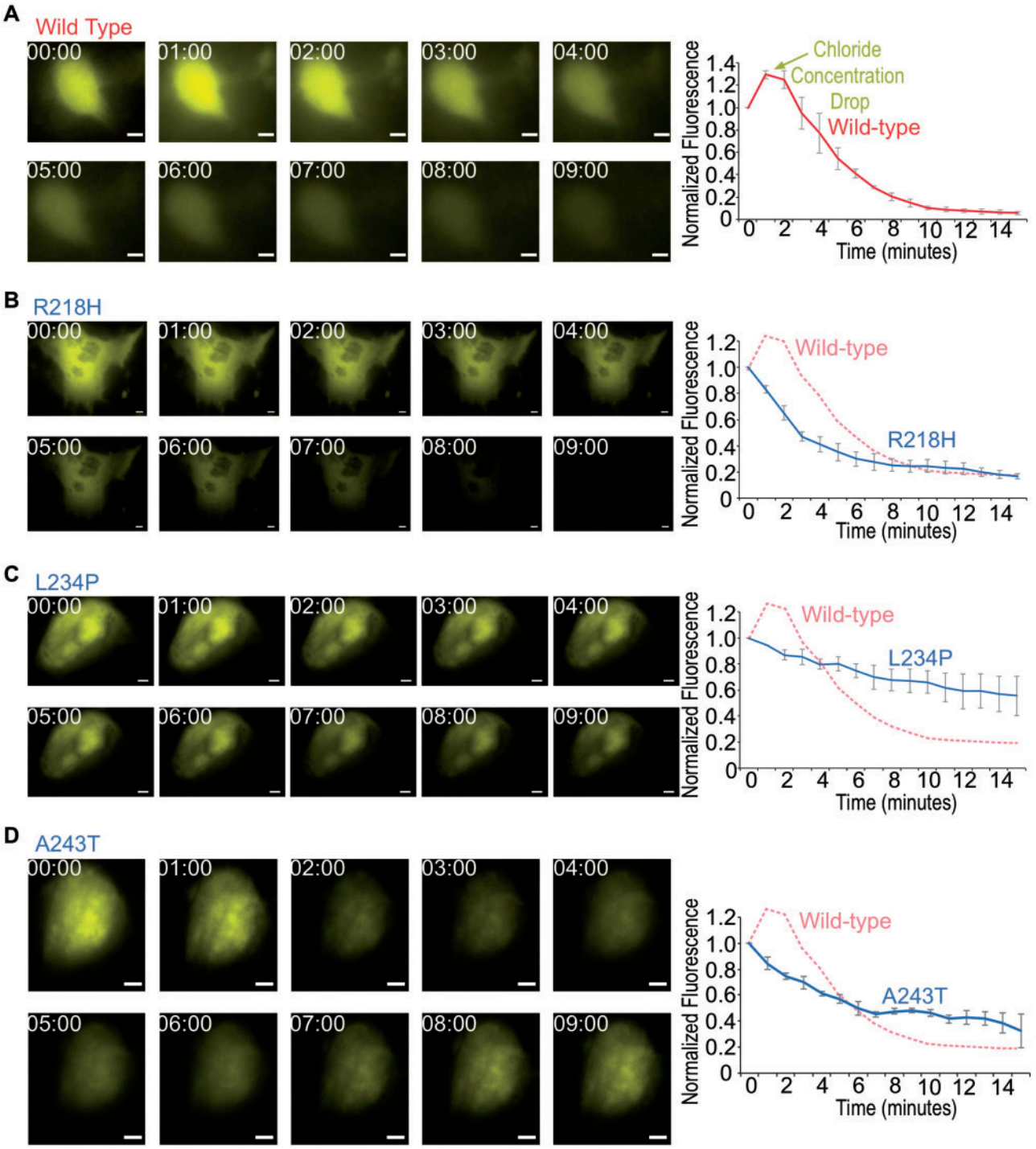


**Figure 3.** Defective $Cl^-$ export in patient-specific iRPE revealed by biosensor imaging following calcium release. Representative still images of WT (**A**), R218H (**B**), L234P (**C**) and A243T (**D**) patient-derived RPE cells expressing $Cl^-$ biosensor and stimulated with 5 μM A23187 (left panels). Images were acquired at the given time in minutes after stimulation. Quantification of mean whole-cell biosensor emission intensity, normalized to $t = 0$ time point (right graphs). Data are represented as mean ± Standard error of the mean. Scale bar = 5 μm.

**Figure 2.** Continued
interface of R105, R218 and T219. The R218H mutation disrupts this binding site. **(F)** Electrostatic potential surfaces of the WT hBEST1 monomer and R218H hBEST1 reveal a change in positive to neutral potential in the residues surrounding the mutation. **(G)** Visualization of the location of L234P mutation in hBEST1. **(H)** Substitution of L234 with a proline would disrupt the secondary structure of the channel pore. Red represents helical residues while green represents residues that form disordered loops.**(I)** Visualization of the location of A243T mutation in hBEST1. **(J)** Hydrophobicity surface representations of the WT hBEST1 monomer and A243T mutant reveal a substitution of a hydrophobic residue to an uncharged, polar amino acid in a helix that is partially embedded in the membrane. The color scheme for the surface hydrophobicity is based on the Kyte and Doolittle scale.

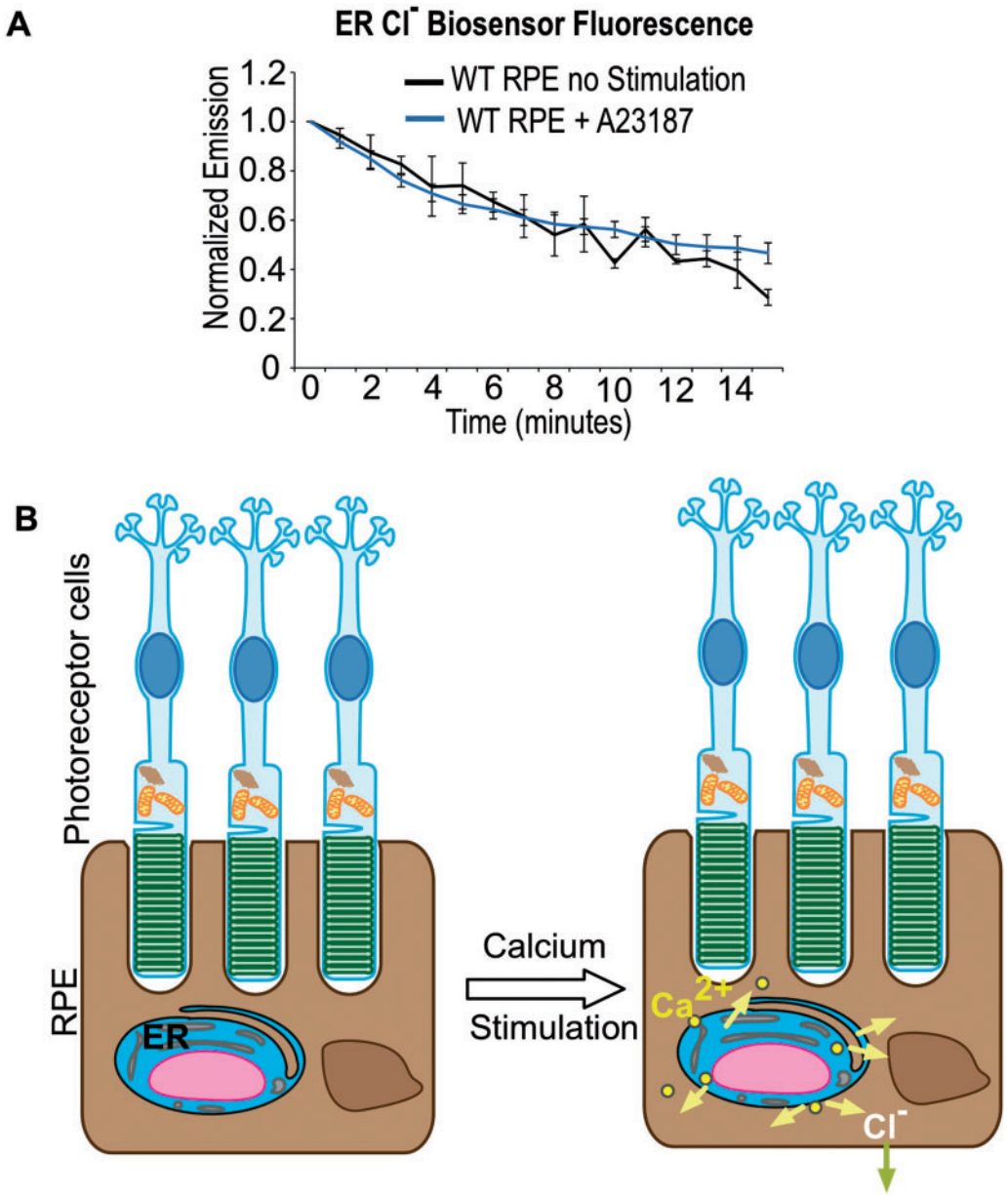


**Figure 4.** BEST1 $Cl^-$ current does not pass through ER. **(A)** Biosensor imaging of ER $Cl^-$ currents. Quantification of mean biosensor emission from WT RPE cells. $Cl^-$ biosensor was targeted to the ER and cells were imaged with and without A23187 stimulation. No significant change in $Cl^-$ ions was found in the ER. **(B)** Model of bestrophin-mediated $Cl^-$ current in RPE cells. Light induced activation of MerTK results in the generation of inositol-1,4,5-trisphosphate which triggers $Ca^{2+}$ release from ER stores (pink arrows) and $Cl^-$ ion outflux (blue arrow).

Secondary antibodies are Alexa Fluor 555 goat anti-rabbit IgG (Invitrogen).

### Biosensor imaging

iRPE cells were seeded on matrigel (BD Biosciences) coated TransWell membranes (Corning). The $Cl^-$ biosensor (pcDNA3.1 EYFP H148Q/I152L) was purchased from Addgene and transfected into RPE cells with Lipofectamine 3000 (Invitrogen). Three days after transfection, individual biosensor-expressing RPE were imaged on a Lieca DM5000B upright fluorescent microscope with SPOT Imaging Solutions software. Cells were stimulated with 5 μM $Ca^{2+}$ ionophore A23187 (IC50 ~ 0.5–1 μM, Sigma, St Louis) (55) in PBS at 37°C and images were taken every minute for 15 min. All images were acquired at 40X magnification with a GFP filter set and 500 ms exposure. Raw images were processed using ImageJ software.

## Supplementary Material

Supplementary Material is available at *HMG* online.

## Acknowledgements

The authors thank Diana Colgan, Melinda Smits and Lokesh Gakhar for technical assistance.

*Conflict of Interest statement*. None declared.

## Funding

The Barbara & Donald Jonas Laboratory of Regenerative Medicine and Bernard & Shirlee Brown Glaucoma Laboratory are supported by the National Institute of Health (5P30EY019007, R01EY018213, R01EY024698, R21AG050437); National Cancer Institute Core (5P30CA013696); the Research to Prevent Blindness (RPB) Physician-Scientist Award; unrestricted funds from RPB, New York, NY, USA. S.H.T. is a member of the RD-CURE Consortium and is supported by the Tistou and Charlotte Kerstan Foundation; the Schneeweiss Stem Cell Fund; New York State (C029572); the Foundation Fighting Blindness New York Regional Research Center Grant (C-NY05-0705-0312); the Joel Hoffman Fund; the Professor Gertrude Rothschild Stem Cell Foundation and the Gebroe Family Foundation. V.B.M. is supported by the National Institutes of Health (K08EY020530, R01EY016822); Doris Duke Charitable Foundation Grant #2013103 and RPB, New York, NY. G.V. is supported by the National Institute of Health (T32GM007337).

## References

1. Berend, K., van Hulsteijn, L.H. and Gans, R.O. (2012) Chloride: the queen of electrolytes? *Eur. J. Intern. Med.*, **23**, 203–211.
2. Marquardt, A., Stohr, H., Passmore, L.A., Kramer, F., Rivera, A. and Weber, B.H. (1998) Mutations in a novel gene, VMD2, encoding a protein of unknown properties cause juvenile-onset vitelliform macular dystrophy (Best's disease). *Hum. Mol. Genet.*, **7**, 1517–1525.
3. Petrukhin, K., Koisti, M.J., Bakall, B., Li, W., Xie, G., Marknell, T., Sandgren, O., Forsman, K., Holmgren, G., Andreasson, S. *et al.* (1998) Identification of the gene responsible for Best macular dystrophy. *Nat. Genet.*, **19**, 241–247.
4. Marmorstein, A.D., Marmorstein, L.Y., Rayborn, M., Wang, X., Hollyfield, J.G. and Petrukhin, K. (2000) Bestrophin, the product of the Best vitelliform macular dystrophy gene (VMD2), localizes to the basolateral plasma membrane of the retinal pigment epithelium. *Proc. Natl Acad. Sci. U. S. A.*, **97**, 12758–12763.
5. Fujii, S., Gallemore, R.P., Hughes, B.A. and Steinberg, R.H. (1992) Direct evidence for a basolateral membrane Cl-conductance in toad retinal pigment epithelium. *Am. J. Physiol.*, **262**, C374–C383.
6. Barro Soria, R., Spitzner, M., Schreiber, R. and Kunzelmann, K. (2009) Bestrophin-1 enables Ca2+-activated Cl-conductance in epithelia. *J. Biol. Chem.*, **284**, 29405–29412.
7. Burgess, R., Millar, I.D., Leroy, B.P., Urquhart, J.E., Fearon, I.M., De Baere, E., Brown, P.D., Robson, A.G., Wright, G.A., Kestelyn, P. *et al.* (2008) Biallelic mutation of BEST1 causes a distinct retinopathy in humans. *Am. J. Hum. Genet.*, **82**, 19–31.
8. Davidson, A.E., Millar, I.D., Urquhart, J.E., Burgess-Mullan, R., Shweikh, Y., Parry, N., O'Sullivan, J., Maher, G.J., McKibbin, M., Downes, S.M. *et al.* (2009) Missense mutations in a retinal pigment epithelium protein, bestrophin-1, cause retinitis pigmentosa. *Am. J. Hum. Genet.*, **85**, 581–592.
9. Xiao, Q., Hartzell, H.C. and Yu, K. (2010) Bestrophins and retinopathies. *Pflugers Arch.*, **460**, 559–569.
10. Kunzelmann, K., Kongsuphol, P., Chootip, K., Toledo, C., Martins, J.R., Almaca, J., Tian, Y., Witzgall, R., Ousingsawat, J. and Schreiber, R. (2011) Role of the Ca2+ -activated Cl-channels bestrophin and anoctamin in epithelial cells. *Biol. Chem.*, **392**, 125–134.
11. Weingeist, T.A., Kobrin, J.L. and Watzke, R.C. (1982) Histopathology of Best's macular dystrophy. *Arch. Ophthalmol.*, **100**, 1108–1114.
12. Cross, H.E. and Bard, L. (1974) Electro-oculography in Best's macular dystrophy. *Am. J. Ophthalmol.*, **77**, 46–50.
13. Marmorstein, L.Y., Wu, J., McLaughlin, P., Yocom, J., Karl, M.O., Neussert, R., Wimmers, S., Stanton, J.B., Gregg, R.G., Strauss, O. *et al.* (2006) The light peak of the electroretinogram is dependent on voltage-gated calcium channels and antagonized by bestrophin (best-1). *J. Gen. Physiol.*, **127**, 577–589.
14. Marmorstein, A.D. and Kinnick, T.R. (2007) Focus on molecules: bestrophin (best-1). *Exp. Eye Res.*, **85**, 423–424.
15. Barro-Soria, R., Schreiber, R. and Kunzelmann, K. (2008) Bestrophin 1 and 2 are components of the Ca(2+) activated Cl(-) conductance in mouse airways. *Biochim. Biophys. Acta*, **1783**, 1993–2000.
16. Marmorstein, A.D., Cross, H.E. and Peachey, N.S. (2009) Functional roles of bestrophins in ocular epithelia. *Prog. Retin. Eye Res.*, **28**, 206–226.
17. Barro-Soria, R., Aldehni, F., Almaca, J., Witzgall, R., Schreiber, R. and Kunzelmann, K. (2010) ER-localized bestrophin 1 activates Ca2+-dependent ion channels TMEM16A and SK4 possibly by acting as a counterion channel. *Pflugers Arch.*, **459**, 485–497.
18. Neussert, R., Muller, C., Milenkovic, V.M. and Strauss, O. (2010) The presence of bestrophin-1 modulates the Ca2+ recruitment from Ca2+ stores in the ER. *Pflugers Arch.*, **460**, 163–175.
19. Hartzell, H.C., Qu, Z., Yu, K., Xiao, Q. and Chien, L.T. (2008) Molecular physiology of bestrophins: multifunctional membrane proteins linked to best disease and other retinopathies. *Physiol. Rev.*, **88**, 639–672.
20. Strauss, O., Muller, C., Reichhart, N., Tamm, E.R. and Gomez, N.M. (2014) The role of bestrophin-1 in intracellular Ca(2+) signaling. *Adv. Exp. Med. Biol.*, **801**, 113–119.
21. Marmorstein, A.D., Kinnick, T.R., Stanton, J.B., Johnson, A.A., Lynch, R.M. and Marmorstein, L.Y. (2015) Bestrophin-1 influences transepithelial electrical properties and Ca2+ signaling in human retinal pigment epithelium. *Mol. Vis.*, **21**, 347–359.
22. Yang, T., Liu, Q., Kloss, B., Bruni, R., Kalathur, R.C., Guo, Y., Kloppmann, E., Rost, B., Colecraft, H.M. and Hendrickson, W.A. (2014) Structure and selectivity in bestrophin ion channels. *Science*, **346**, 355–359.
23. Singh, R., Shen, W., Kuai, D., Martin, J.M., Guo, X., Smith, M.A., Perez, E.T., Phillips, M.J., Simonett, J.M., Wallace, K.A. *et al.* (2013) iPS cell modeling of Best disease: insights into the pathophysiology of an inherited macular degeneration. *Hum. Mol. Genet.*, **22**, 593–607.
24. Wright, L.S., Phillips, M.J., Pinilla, I., Hei, D. and Gamm, D.M. (2014) Induced pluripotent stem cells as custom therapeutics for retinal repair: progress and rationale. *Exp. Eye Res.*, **123**, 161–172.
25. Milenkovic, A., Brandl, C., Milenkovic, V.M., Jendryke, T., Sirianant, L., Wanitchakool, P., Zimmermann, S., Reiff, C.M., Horling, F., Schrewe, H. *et al.* (2015) Bestrophin 1 is indispensable for volume regulation in human retinal pigment epithelium cells. *Proc. Natl Acad. Sci. U. S. A.*, **112**, E2630–E2639.
26. Li, Y., Chan, L., Nguyen, H.V. and Tsang, S.H. (2016) Personalized medicine: cell and gene therapy based on

patient-specific iPSC-derived retinal pigment epithelium cells. *Adv. Exp. Med. Biol.*, **854**, 549–555.
27. Nguyen, H.V., Li, Y. and Tsang, S.H. (2015) Patient-specific iPSC-derived RPE for modeling of retinal diseases. *J. Clin. Med.*, **4**, 567–578.
28. Stohr, H., Marquardt, A., Nanda, I., Schmid, M. and Weber, B.H. (2002) Three novel human VMD2-like genes are members of the evolutionary highly conserved RFP-TM family. *Eur. J. Hum. Genet.*, **10**, 281–284.
29. Boon, C.J., Klevering, B.J., Leroy, B.P., Hoyng, C.B., Keunen, J.E. and den Hollander, A.I. (2009) The spectrum of ocular phenotypes caused by mutations in the BEST1 gene. *Prog. Retin. Eye Res.*, **28**, 187–205.
30. Kane Dickson, V., Pedi, L. and Long, S.B. (2014) Structure and insights into the function of a Ca(2+)-activated Cl(-) channel. *Nature*, **516**, 213–218.
31. Galietta, L.J., Haggie, P.M. and Verkman, A.S. (2001) Green fluorescent protein-based halide indicators with improved chloride and iodide affinities. *FEBS Lett.*, **499**, 220–224.
32. Babcock, D.F., First, N.L. and Lardy, H.A. (1976) Action of ionophore A23187 at the cellular level. Separation of effects at the plasma and mitochondrial membranes. *J. Biol. Chem.*, **251**, 3881–3886.
33. Constable, P.A. (2014) A perspective on the mechanism of the light-rise of the electrooculogram. *Invest. Ophthalmol. Vis. Sci.*, **55**, 2669–2673.
34. Reichhart, N. and Strauß, O. (2014) Ion channels and transporters of the retinal pigment epithelium. *Exp. Eye Res.*, **126**, 27–37.
35. Okiyoneda, T. and Lukacs, G.L. (2012) Fixing cystic fibrosis by correcting CFTR domain assembly. *J. Cell Biol.*, **199**, 199–204.
36. Mezghrani, A., Monteil, A., Watschinger, K., Sinnegger-Brauns, M.J., Barrere, C., Bourinet, E., Nargeot, J., Striessnig, J. and Lory, P. (2008) A destructive interaction mechanism accounts for dominant-negative effects of misfolded mutants of voltage-gated calcium channels. *J. Neurosci.*, **28**, 4501–4511.
37. Milenkovic, V.M., Rohrl, E., Weber, B.H. and Strauss, O. (2011) Disease-associated missense mutations in bestrophin-1 affect cellular trafficking and anion conductance. *J. Cell Sci.*, **124**, 2988–2996.
38. Yu, K., Cui, Y. and Hartzell, H.C. (2006) The bestrophin mutation A243V, linked to adult-onset vitelliform macular dystrophy, impairs its chloride channel function. *Invest. Ophthalmol. Vis. Sci.*, **47**, 4956–4961.
39. Mullins, R.F., Oh, K.T., Heffron, E., Hageman, G.S. and Stone, E.M. (2005) Late development of vitelliform lesions and flecks in a patient with best disease: clinicopathologic correlation. *Arch. Ophthalmol.*, **123**, 1588–1594.
40. Caldwell, G.M., Kakuk, L.E., Griesinger, I.B., Simpson, S.A., Nowak, N.J., Small, K.W., Maumenee, I.H., Rosenfeld, P.J., Sieving, P.A., Shows, T.B. *et al.* (1999) Bestrophin gene mutations in patients with Best vitelliform macular dystrophy. *Genomics*, **58**, 98–101.
41. Marchant, D., Gogat, K., Boutboul, S., Pequignot, M., Sternberg, C., Dureau, P., Roche, O., Uteza, Y., Hache, J.C., Puech, B. *et al.* (2001) Identification of novel VMD2 gene mutations in patients with best vitelliform macular dystrophy. *Hum. Mutat.*, **17**, 235.
42. Atchaneeyasakul, L.O., Jinda, W., Sakolsatayadorn, N., Trinavarat, A., Ruangvoravate, N., Thanasombatskul, N., Thongnoppakhun, W. and Limwongse, C. (2008) Mutation analysis of the VMD2 gene in thai families with best macular dystrophy. *Ophthalmic Genet.*, **29**, 139–144.
43. Yang, T., Justus, S., Li, Y. and Tsang, S.H. (2015) BEST1: the best target for gene and cell therapies. *Mol. Ther.*, **23**, 1805–1809.
44. Frambach, D.A., Roy, C.E., Valentine, J.L. and Weiter, J.J. (1989) Precocious retinal adhesion is affected by furosemide and ouabain. *Curr. Eye Res.*, **8**, 553–556.
45. Bassuk, A.G., Sujirakul, T., Tsang, S.H. and Mahajan, V.B. (2014) A novel RPGR mutation masquerading as Stargardt disease. *Br. J. Ophthalmol.*, **98**, 709–711.
46. Duncker, T., Greenberg, J.P., Ramachandran, R., Hood, D.C., Smith, R.T., Hirose, T., Woods, R.L., Tsang, S.H., Delori, F.C. and Sparrow, J.R. (2014) Quantitative fundus autofluorescence and optical coherence tomography in best vitelliform macular dystrophy. *Invest. Ophthalmol. Vis. Sci.*, **55**, 1471–1482.
47. Eswar, N., Webb, B., Marti-Renom, M.A., Madhusudhan, M.S., Eramian, D., Shen, M.Y., Pieper, U. and Sali, A. (2007) Comparative protein structure modeling using MODELLER. *Curr. Protoc. Protein Sci.*, **50**, 2.9: 2.9.1-2.9.31.
48. Bassuk, A.G., Yeh, S., Wu, S., Martin, D.F., Tsang, S.H., Gakhar, L. and Mahajan, V.B. (2015) Structural modeling of a novel CAPN5 mutation that causes uveitis and neovascular retinal detachment. *PLoS One*, **10**, e0122352.
49. Pettersen, E.F., Goddard, T.D., Huang, C.C., Couch, G.S., Greenblatt, D.M., Meng, E.C. and Ferrin, T.E. (2004) UCSF chimera–a visualization system for exploratory research and analysis. *J. Comput. Chem.*, **25**, 1605–1612.
50. Sehnal, D., Svobodova Varekova, R., Berka, K., Pravda, L., Navratilova, V., Banas, P., Ionescu, C.M., Otyepka, M. and Koca, J. (2013) MOLE 2.0: advanced approach for analysis of biomacromolecular channels. *J. Cheminform.*, **5**, 39.
51. Baker, N.A., Sept, D., Joseph, S., Holst, M.J. and McCammon, J.A. (2001) Electrostatics of nanosystems: application to microtubules and the ribosome. *Proc. Natl Acad. Sci. U. S. A.*, **98**, 10037–10041.
52. Kearse, M., Moir, R., Wilson, A., Stones-Havas, S., Cheung, M., Sturrock, S., Buxton, S., Cooper, A., Markowitz, S., Duran, C. *et al.* (2012) Geneious basic: an integrated and extendable desktop software platform for the organization and analysis of sequence data. *Bioinformatics*, **28**, 1647–1649.
53. Li, Y., Tsai, Y.T., Hsu, C.W., Erol, D., Yang, J., Wu, W.H., Davis, R.J., Egli, D. and Tsang, S.H. (2012) Long-term safety and efficacy of human-induced pluripotent stem cell (iPS) grafts in a preclinical model of retinitis pigmentosa. *Mol. Med.*, **18**, 1312–1319.
54. Bock, C., Kiskinis, E., Verstappen, G., Gu, H., Boulting, G., Smith, Z.D., Ziller, M., Croft, G.F., Amoroso, M.W., Oakley, D.H. *et al.* (2011) Reference maps of human ES and iPS cell variation enable high-throughput characterization of pluripotent cell lines. *Cell*, **144**, 439–452.
55. Hall, M.O., Abrams, T.A. and Mittag, T.W. (1991) ROS ingestion by RPE cells is turned off by increased protein kinase C activity and by increased calcium. *Exp. Eye Res.*, **52**, 591–598.